PAPER

300-GHz-Band Dual-Band Bandstop Filter Based on Two Different Sized Split Ring Resonators

Akihiko HIRATA[†a)], ***Senior Member***

SUMMARY For 6G mobile communications, it is important to realize a 300 GHz band bandpass filter that fits the occupied bandwidth of wireless communication system to prevent inter-system interference. This paper presents the design of a 300-GHz-band dual-band bandstop filter composed of two types of different sized split ring resonator (SRR) unit cells. The SRR unit cells are formed by a 5-μm-thick gold pattern on a 200-μm-thick quartz substrate. When two different-sized SRR unit cells are placed alternately on the same quartz substrate and the SRR unit cell size is over 260 μm, the stopbands of the dual-band bandstop filter are almost the same as those of the bandstop filter, which is composed of a single SRR unit cell. The insertion loss of the dual-band bandstop filter at 297.4 GHz is 1.8 dB and the 3-dB passband becomes 16.0 GHz (290.4–306.4 GHz). The attenuation in the two stopbands is greater than 20 dB. Six types of dual-band bandstop filters with different arrangement and different distance between SRR unit cells are prototyped, and the effect of the distance and arrangement between different sized SRR unit cells on the transmission characteristics of dual-band bandstop filters were clarified.

key words: *millimeter-wave wireless communications, bandstop filter, bandpass filter, metasurface*

1. Introduction

The research and development of a 300-GHz-band wireless link has become an active means for achieving >100-Gbit/s data rate in the 6th generation (6G) mobile communication system [1]–[6]. In the 300-GHz-band wireless communication system, terahertz (THz) band multiple bandstop filters are required to suppress the interference between other wireless systems [7]. Several THz band filters, such as waveguide bandpass filters (BPFs) [8]–[10] and photonic crystal BPFs [11], have been proposed. However, these THz band filters require sub-millimeter-wave order three-dimensional (3D) fabrication and are difficult to manufacture as designed.

THz band filters that employ metasurfaces have been investigated because they can be fabricated using a simple fabrication process [12]–[14]. In particular, split ring resonators (SRR) are attracting a great deal of interest as a way to achieve THz filters. An SRR can achieve abnormal electromagnetic properties, such as a negative refractive index. The SRR is composed of metallic rings with gaps, and it has resonance related to the inductive-capacitive coupling of the circulating currents [15]–[17]. In particular, various types of bandpass and bandstop filters that employ SRR have been reported [18]–[23]. Several THz-band SRR bandpass filters have been reported [24], [25]. However, these filters require a multi-layer fabrication process, their pass band is quite broad (>20%), and it is difficult for them to be used to suppress undesired interference between co-existing wireless channels in THz wireless communication systems. One way to achieve a narrow-band THz BPF is to use a dual-band bandstop filter based on a metasurface. Several dual-band bandstop filters operating in the THz band have been reported. Junlin et al. reported a metamaterial-based dual-band bandstop filter, whose unit cell comprised a dual-band electric-field-coupled resonator [26]. Metamaterial-based dual-band THz filters composed of two different unit cells have been reported [27]–[29]. However, the two stopband differences of these THz dual-band filters are large, making them unsuitable for suppressing undesired interference between co-existing wireless channels in THz wireless communication systems. Moreover, there were few studies that examined in detail the effect of the spacing and arrangement between the two different sized unit cells on the transmission characteristics of the filter.

The purpose of this paper is to establish a design theory for dual-band bandstop filters composed of different sized SRR unit cells by clarifying the effect of the distance and arrangement between different sized SRR unit cells on the transmission characteristics of dual-band bandstop filters. In this study, we investigate the design of a dual-band bandstop filter by arranging SRR unit cells of two different sizes on the same quartz substrate. Previously, the author reported a 120-GHz-band single-mode SRR bandstop filter made of 5-μm-thick gold on a 200-μm-thick quartz substrate. The insertion loss of this filter was 37.8 dB at 124.8 GHz, and −10-dB bandwidth of the bandstop filter was approximately 14 GHz [28], [29]. Our objective is to realize a dual-band bandstop filter that allows the spacing between the two stopbands to be set to the desired frequency by using these two SRR unit cells of different sizes. First, the design of the SRR bandstop filter is explained. Second, the simulation and experimental results of the designed SRR bandstop filter are presented. Subsequently, the designing of the dual-band bandstop filters are presented, where the filters composed of two different-sized SRR unit cells, and the dependence of transmission characteristics on the arrangement of two different sized SRR unit cells are evaluated by simulation and experiments.

Manuscript received February 6, 2023.
Manuscript revised May 15, 2023.
Manuscript publicized October 13, 2023.

[†]The author is with the Dept. of Information and Communication Systems Engineering, Chiba Institute of Technology, Narashino-shi, 275–0016 Japan.
a) E-mail: hirata.akihiko@p.chibakoudai.jp

DOI: 10.1587/transele.2023ECP5004

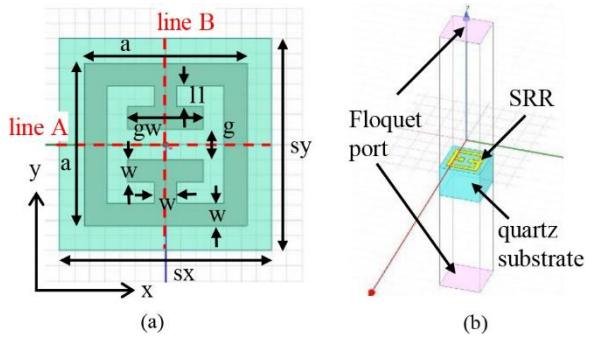

Fig. 1 (a) Schematic of the SRR unit cell. (b) Simulation model for an SRR bandstop filter.

2. Design of SRR Bandstop Filter

Figure 1 (a) illustrates the simulation model of the SRR unit cell used for the SRR bandstop filter, whose stopband range from 280 to 320 GHz. SRR unit cells are made of 5-μm-thick gold on a 200-μm-thick quartz substrate. The permittivity and loss tangent of the quartz are 3.5 and 0.0001, respectively. The conductivity of gold is 4.1 x 10^7 s/m.

The size of the unit cell along the x-axis (sx) and y-axis (sy) is 220 μm, 260 μm, and 300 μm, the capacitor gap (g) is 32 μm, and the linewidth (w) is 25 μm. The SRR side length (a), capacitor line length ($l1$) and capacitor length (gw) depends on the resonant frequency of the SRR unit cell. Figure 1 (b) displays the simulation model for the full 3D electromagnetic (EM) simulations based on the finite element method (ANSYS HFSS). For the simulation of a planar periodic structure of the SRR unit cells, we used a simulation model with a floquet port. The floquet port in the HFSS is used exclusively with planar-periodic structures [30]. The electric field of the plane wave is parallel to the y axis in Fig. 1 (a). In this case, the electric coupling is dominant between the SRRs as it is aligned parallel to the y-axis, and magnetic coupling is dominant between the SRRs aligned parallel to the x-axis.

Figure 2 presents the simulation results of the SRR bandstop filter, whose size parameter is listed in Table 1. The unit cell sizes (sx and sy) are 220, 260, and 300 μm, respectively. As the unit cell size (sx and sy) increase, the SRR side length (a) increases. This is because the resonant frequency of the SRR is proportional to $1/\sqrt{LC}$, and the capacitance between adjacent SRRs decreases as the unit cell size increases. Consequently, the SRR side length should be lengthened to compensate for the decrease in the capacitance and to maintain the resonant frequency at 300 GHz. S_{21} of these bandstop filters decreases as the cell size increases, when the separation frequency away from the resonance frequency is the same. The unloaded quality factor of SRR calculated from the simulation results shown in Fig. 2 (a) is about 112 for all SRRs with cell sizes of 220, 260 and 300 μm. The 10-dB bandwidth increases as the unit cell size decreases. The 10-dB bandwidth for the model with a cell size of 220 μm was more than 59.2 GHz. When the unit cell

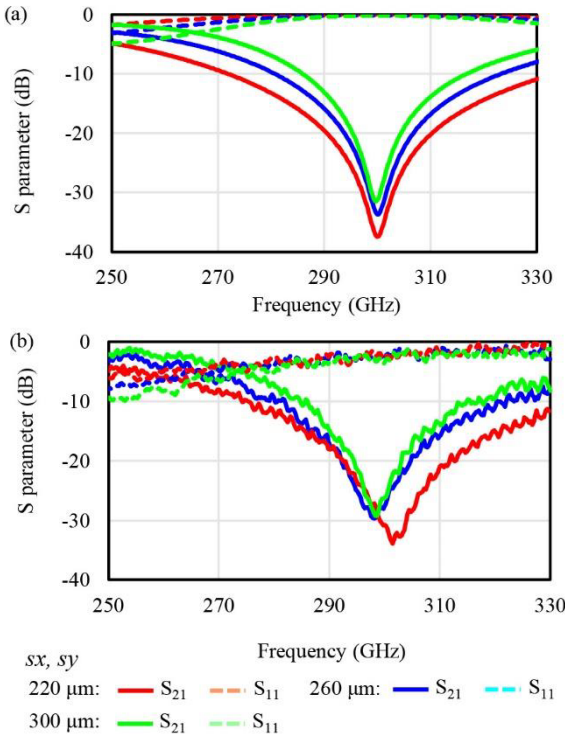

Fig. 2 Simulation results (a) and experimental results (b) of S parameter characteristics of SRR bandstop filter as a parameter of unit cell size (sx, sy).

Table 1 SRR size parameters of 300-GHz-band bandstop SRR filter. Unit is μm.

Frequency	a	g	w	$l1$	gw	sx,sy
300GHz	184.0	32	25	26.0	41.2	220.0
300GHz	202.6	32	25	35.3	41.6	260.0
300GHz	204.6	32	25	36.3	41.6	300.0

size was 300 μm, the 10-dB bandwidth was approximately 29.7 GHz.

We prototyped the SRR bandstop filters listed in Table 1 and evaluated their transmission characteristics using a vector network analyzer (VNA). We employed a 200 μm thick quartz substrate, and the thickness of the gold film was approximately 5 μm. The manufacturing process was carried out according to the following procedures. First, Ti/Pd thin film was formed on the quartz substrate. After resist coating and resist pattern formation, SRR patterns are formed by gold plating. Next, after stripping the resist, the unnecessary Ti/Pd thin film is removed by etching.

Photographs of the SRR with unit cell sizes (sx and sy) of 220, 260, and 300 μm are shown in Fig. 3 (a), 3 (b), and 3 (c), respectively. A photograph of the experimental setup is displayed in Fig. 4. The measurements were performed by connecting a frequency extender (VDI WR3.4-VNAX) to a VNA (Keysight PNA-X). THz waves were emitted from an orthogonal horn antenna attached to a frequency extender and received by another orthogonal horn antenna. The gain of the orthogonal horn antenna is 25 dBi at 300 GHz. The

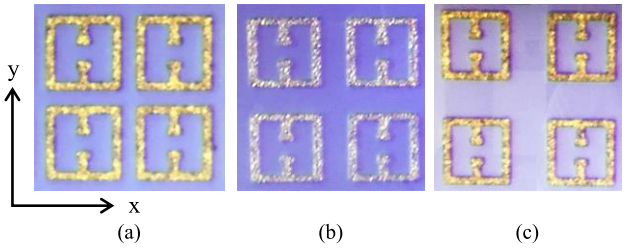

Fig. 3 Photographs of the SRR with the unit cell sizes of (a) 220 μm, (b) 260 μm, and (c) 300 μm.

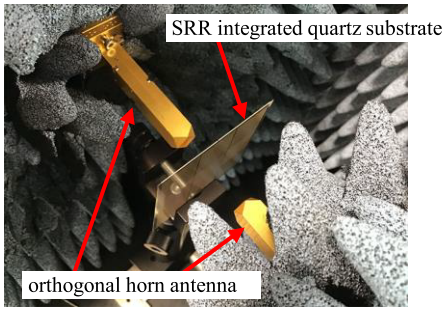

Fig. 4 Photographs of the experimental setup for the transmission characteristic evaluation of SRR bandstop filter.

measured S parameters of the SRR bandstop filter are presented in Fig. 2 when the electric field of the incident wave is parallel to the y axis, as shown in Fig. 1 (a). The simulation and experimental results agreed well with each other. The unloaded quality factor of SRR calculated from the experimental results shown in Fig. 2 (b) is about 84 for SRR with cell sizes of 220 μm, about 67 with cell sizes of 260 μm, and about 99 with cell sizes of 300 μm.

As presented in Fig. 2 and Table 1, the unit cell size of the SRR affects the stopband of the SRR filter owing to the magnetic and electric coupling between the adjacent SRRs in the x- and y-axis directions, respectively. We simulated the dependence of the stopband of the SRR filter on the distance between adjacent SRRs in the x- and y-directions. Figure 5 illustrates the simulation results of the SRR bandstop filter characteristics as a function of the unit cell size. In these simulations, the SRR side length (a) was 202.6 μm and capacitor length (gw) was 41.6 μm. The stopband of the SRR filter was 300 GHz when both sx and sy were 260 μm. When sx increases from 200 μm to 260 μm and sy remained constant (260 μm), the stopband of the SRR filter changed from 286 GHz to 300 GHz (Fig. 5 (a)). However, sx increases from 260 μm to 380 μm, the stopband has decreased slightly from 300 GHz to 297 GHz. In the case of the y-axis direction, the stopband of the SRR filter changes over 50 GHz as sy increases from 200 μm to 260 μm, and sx is constant (260 μm) (Fig. 5 (b)). The stopband varies in the range of 297 GHz to 305 GHz, in case sy increases from 260 μm to 380 μm. In case the cell size increases in both of x-axis and y-axis direction (Fig. 5 (c)), the stopband of the SRR filter changes over 50 GHz as sx and sy increases from 200 μm to 260 μm, and the stopband varies in the range of 300 GHz to

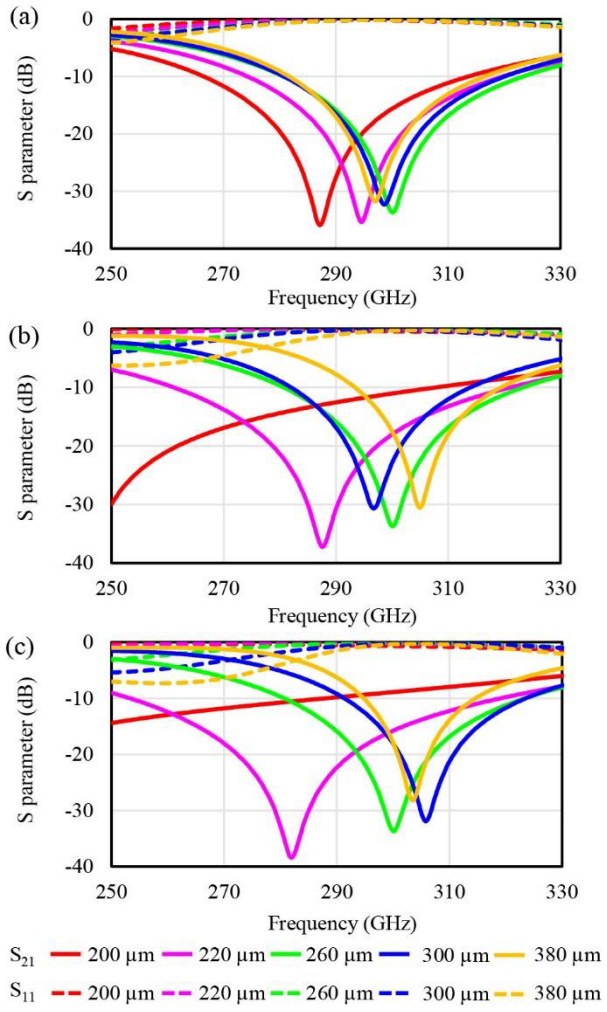

Fig. 5 Simulation results of the SRR bandstop filter characteristics as a parameter of the unit cell size (a) in the x-axis direction and (b) in the y-axis direction, and (c) in both of x-axis and y-axis direction.

306 GHz, in case sx/sy increases from 260 μm to 380 μm. These results indicate that the electric coupling between adjacent SRRs in the x-axis direction affects the stopbands of the SRR filter more than the magnetic coupling between adjacent SRR in the y-axis direction when the unit cell size is less than 260 μm. Thus, when sx/sy exceeds 260 μm, where the influence of electrical and magnetic coupling becomes small, there is no specific trend in the relationship between sx/sy and resonant frequency. We will continue to investigate the reason of these resonant frequency behavior when sx/sy is above 260 μm.

3. Design of Dual-Band SRR Bandstop Filter

We investigated the achievement of a dual-band bandstop filter using these two SRR unit cells with different stopbands. We designed a dual-band bandstop filters using two different sized SRR unit cells, and evaluated their transmission characteristics by 3D electromagnetic simulation. The two types of unit cells were arranged in a checkered pattern,

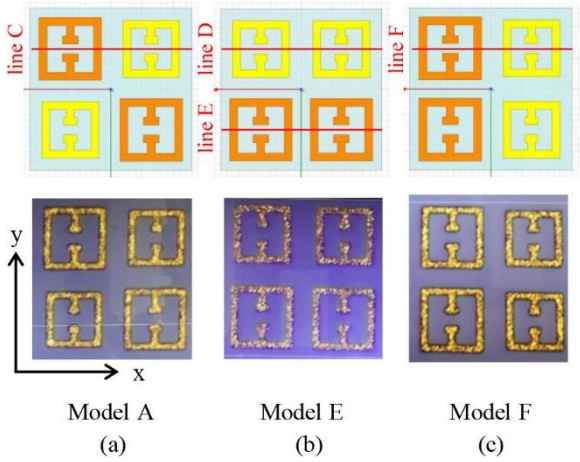

Fig. 6 Schematics and photograph of the dual-band SRR bandstop filters (Model A, Model E, and Model F).

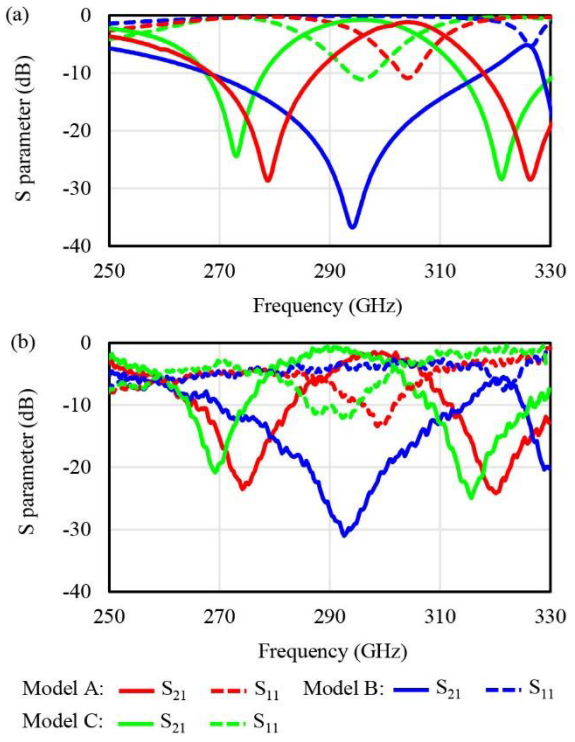

Fig. 7 Simulation (a) and experimental results (b) of S_{21} of dual-band SRR bandstop filters whose unit cell size is 260 μm (Model A), 220 μm (Model B), and 300 μm (Model C).

as illustrated in Fig. 6 (Model A). The design stopbands of the orange and yellow SRR unit cells were 280 GHz and 320 GHz, respectively.

First, we investigate the dependence of the dual-band bandstop filter transmission characteristics on unit cell size. Figure 7 presents the simulation results of S_{21} of the dual-band SRR bandstop filters composed of 280 GHz and 320 GHz SRR unit cells. The unit cell sizes were 260 μm (Model A), 220 μm (Model B), and 300 μm (Model C). The SRR unit cell size parameters of Models A, B, and C

Table 2 SRR size parameter of Model A-E. Unit is μm.

Model	Freq.	*a*	*g*	*w*	*l1*	*gw*	*sx,sy*
A,E,F	280GHz	201.0	32	25	34.5	50.0	260
	320GHz	182.2	32	25	25.1	41.6	260
B	280GHz	193.0	32	25	30.5	41.2	220
	320GHz	181.0	32	25	24.5	41.2	220
C	280GHz	204.0	32	25	36.0	50.0	300
	320GHz	183.2	32	25	25.6	41.6	300
D	295GHz	194.6	32	25	31.3	47.6	260
	305GHz	188.4	32	25	28.2	41.6	260

are listed in Table 2. The unit cell parameters for the 280-GHz-band SRR and 320-GHz-band SRR were determined to demonstrate stopbands at 280 GHz and 320 GHz when the bandstop filter comprised a single sized SRR. The stopbands of Model A were 278 and 326 GHz, and those of Model C were 272 and 319 GHz, respectively. However, unlike Models A and C, only one stopband (293 GHz) was observed in the frequency range of 250 GHz to 330 GHz for Model B. The measurement results of S_{21} for Models A, B, and C are shown in Fig. 7. In Model A, the stopbands were 274 and 320 GHz. The insertion loss of Model A at 297 GHz was 1.8 dB, and the 3-dB passband was 16 GHz (290–306 GHz). This result indicates that Model A can be used as a BPF with a passband of 300 GHz. In the case of Model C, the stopbands were 268 and 317 GHz. In Model B, the stopband is 292 GHz, and the higher stopband is more than 330 GHz. The trends in the simulation and experimental results are roughly in agreement. These results indicate that the stopbands of Models A and C roughly match the stopband of the SRR unit cells that make up Model A or Model C. However, the stopbands of Model B are significantly different from the stopbands of the SRR unit cells that constitutes Model B. The insertion loss of Model C at the pass band is larger than that of Model A. As shown in Fig. 2, insertion loss of the bandstop filter composed of single SRRs decreases as the cell size increases, when the separation frequency away from the resonance frequency is the same. We suppose that S_{21} of Model C at the intermediate frequency (passband) between the two stopbands is larger than that of Model A, because Model C has a larger unit cell size than Model A.

The simulation results of the H fields of Models A, B, and C along line C in Fig. 6 (a) are illustrated in Fig. 8. At the stop bands, no magnetic coupling is observed between the adjacent SRR unit cells along line C in Models A, B, and C because the stopbands of adjacent SRR unit cells along line C are different. The simulation results of the E field of Models A-C are depicted in Fig. 9. A strong electric coupling was observed between the SRRs in the y- axis direction in Model B compared with Models A and C at the stopbands. These results indicate that the stopbands of Model B, unlike Models A and C, are significantly different from the stopband of the SRR unit cells that make up Model B because of the electric field coupling between SRRs in the y-axis direction.

Subsequently, we investigate the control of the pass

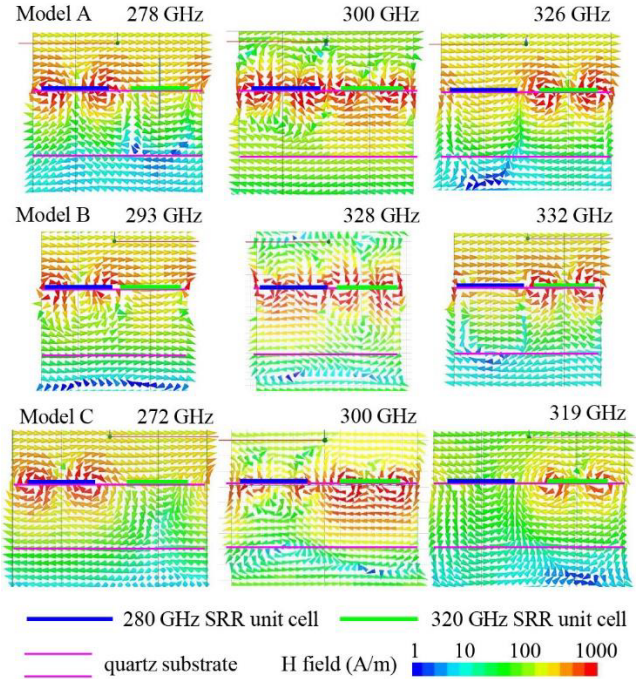

Fig. 8 Simulation results of the H field of Model A-C along the line C shown in Fig. 6 (a) at the stopbands.

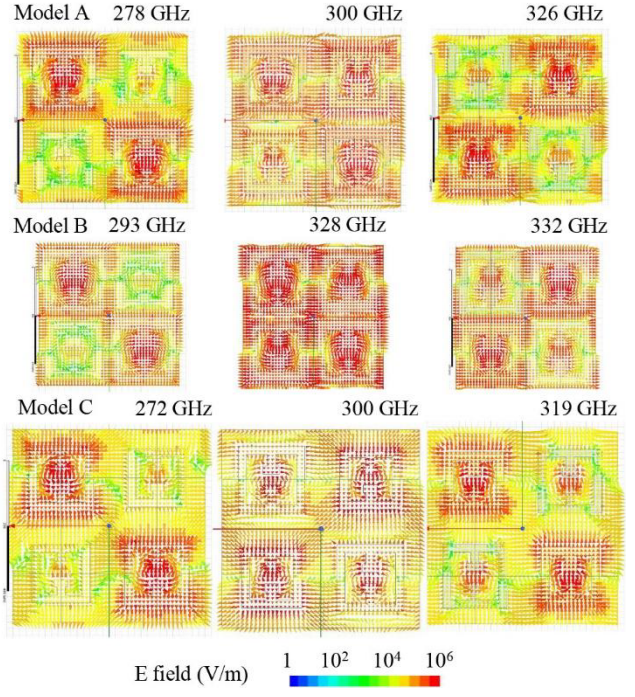

Fig. 9 Simulation results of E-field of dual-band SRR bandstop filters (Model A-C) at stopbands.

bandwidth of the dual-band SRR bandstop filter by selecting the SRR unit cells that comprise the dual-band SRR bandstop filter. We prototyped dual-band SRR bandstop filters composed of 280 GHz and 320 GHz SRR unit cells (Model A), and 295 GHz and 305 GHz SRR unit cells (Model D), and

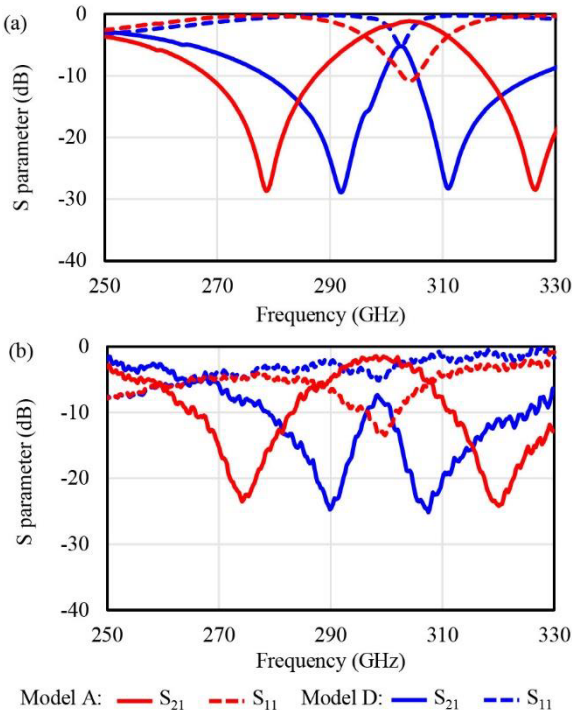

Fig. 10 Simulation (a) and experimental results (b) of S_{21} of dual-band SRR bandstop filters (Model A, Model D).

evaluated their transmission characteristics using VNA. The unit cell size is 260 μm. The SRR unit cell size parameters of the Models A and D are listed in Table 2.

The experimental results of the transmission characteristics of Models A and D are depicted in Fig. 10. In the case of Model A, the lower stopband of the bandstop filters is 274 GHz and the higher stopband is 320 GHz. These stopbands are approximately 0.5~6 GHz lower than those of each SRR unit cell (280 GHz and 320 GHz) that comprises Model A. In the case of Model D, the lower stopband of the bandstop filters is 290 GHz and the higher stopband is 307 GHz. The lower stopband is 5 GHz lower than that of the SRR unit cells (295 GHz), and the higher stopband is 2 GHz higher than that of the SRR unit cell (305 GHz). The simulation results for the transmission characteristics of Models A and D are shown in Fig. 10. The stopbands of the experimental results are approximately 2– 4 GHz lower than those of the simulation results; however, the tendency of the frequency characteristics of both is almost the same. These results indicate that we can control the pass bandwidth of the dual-band SRR bandstop filter by selecting SRR unit cells that comprise the dual-band SRR bandstop filter. However, when the stopband spacing is set as narrow as 10 GHz, as in Model D, the transmission loss at the passband becomes large, approximately 8 dB.

Finally, we investigate the dependence of the transmission characteristics on the arrangement of the SRR unit cells. To this end, we designed three types of dual-band SRR bandstop filters (Models A, E, and F). Schematics and photographs of Models A, E, and F are displayed in Fig. 6.

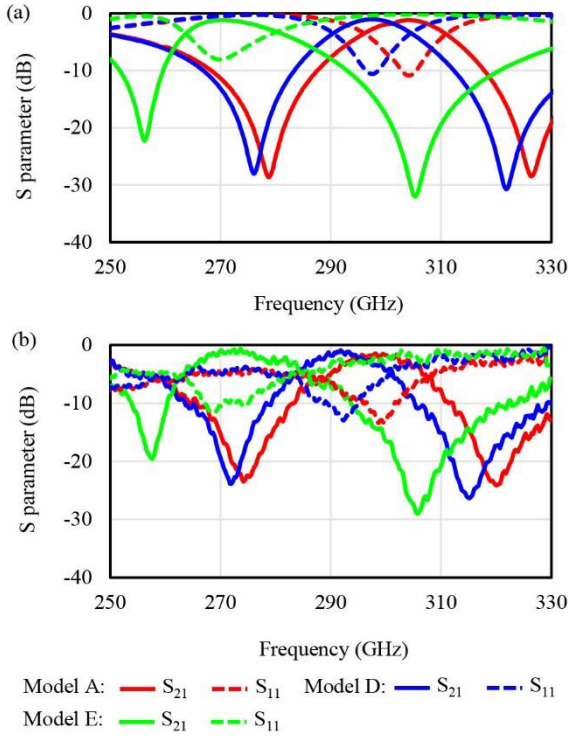

Fig. 11 Simulation (a) and experimental results (b) of S_{21} of the dual-band SRR bandstop filters (Models A, E, and F).

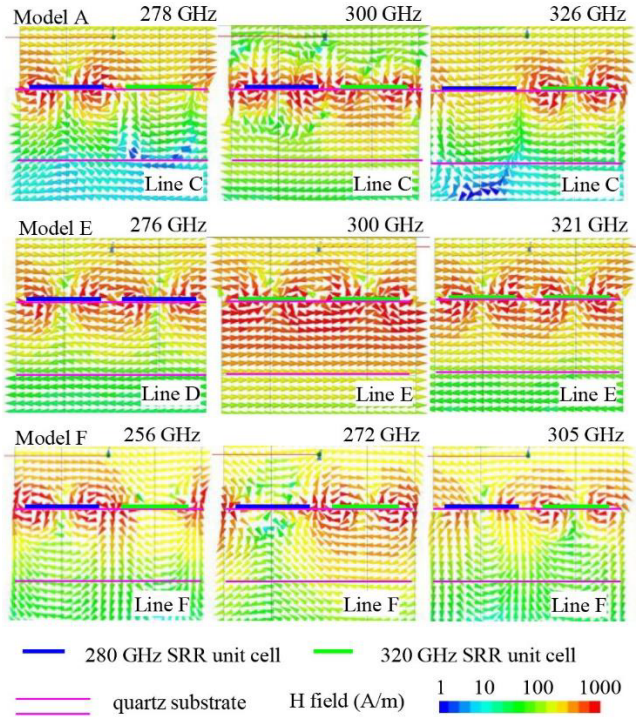

Fig. 12 Simulation results of the H field of Models A, E, and F along the line C-F shown in Fig. 6.

These dual-band SRR bandstop filters are composed of two types of SRR unit cell. The stopbands of the SRR unit cells used for Models A, E, and F were composed of two different sized SRR unit cells whose stopband is 280 and 320 GHz. In Model A, the same types of SRR unit cells were arranged diagonally. The same types of SRR unit cells were arranged parallel to the x- and y-axes shown in Fig. 6 for Models E and F, respectively.

Figure 11 shows the simulation results of S_{21} for Models A, E, and F. In Model A, the lower and higher stopbands are 278 and 326 GHz, respectively. The lower and higher stopbands for Model E are 276 and 321 GHz, respectively. These results indicate that the lower stopband of Model E, in which the same sized SRR unit cells are arranged parallel to the y-axis, is 2–5 GHz lower than that of Model A, in which the same sized SRR unit cells are arranged diagonally. However, the trends in the frequency characteristics for Models A and E are generally the same. The frequency characteristics of Model F differ from those of Models A and E. The lower and higher stopbands are 256 and 305 GHz, respectively, and the stopbands of the dual-band filter are shifted to approximately 14 GHz lower than the stopbands of the two SRR unit cells (280 GHz and 320 GHz) that constitute Model F.

The measurement results of the transmission characteristics of Models A, E, and F are shown in Fig. 11. The measured stopbands of Models A and E were 4–6 GHz lower than the simulated stopbands. In Model F, the measurement and simulation results are almost the same. Figures 12 presents the simulation results of the H field distributions of Models A, E, and F. In the case of Model A, no strong magnetic coupling is observed between the adjacent SRR unit cells along line C at the stopbands, because the stopbands of the adjacent SRR unit cells along line C are different. In Model E, the stopbands of the adjacent SRR unit cells along lines D and E are the same, and strong magnetic coupling between adjacent cells is observed. In Model F, unlike in Models A and E, magnetic coupling is observed between adjacent SRRs along line F, even though the stopbands of the adjacent SRRs are different. Figures 13 presents the simulation results of the E-field distributions of Models A, E, and F. Strong electric coupling between the SRRs at the stopbands in the y-axis direction in Model F is observed compared to Models A and E. Figures 14 shows the simulation results of the surface current flow of Models A, E, and F. In Models A and E, there is almost no circulating current flow in the 280-GHz-band SRR unit cells at the higher stopband, and almost no circulating current in the 320-GHz-band SRR unit cells at the lower stopband. In contrast, in Model F, a weak circulating current flows in the 280-GHz-band SRR unit cells at the higher stopbands and in the 320-GHz-band SRR unit cells at the lower stopband. The strong resonance current induced in the 280 GHz band SRR also induces a resonance current in the 320 GHz band SRR, however, since the resonance frequency of the 320 GHz band SRR is very different from the original resonance frequency of the 320 GHz band SRR, we believe that only weak resonance current flows in the 320 GHz band SRR at 256 GHz. As shown in Figs. 12, 13, and 14, the resonant modes of Model F are different from those of Models A and E. The frequency characteristics of

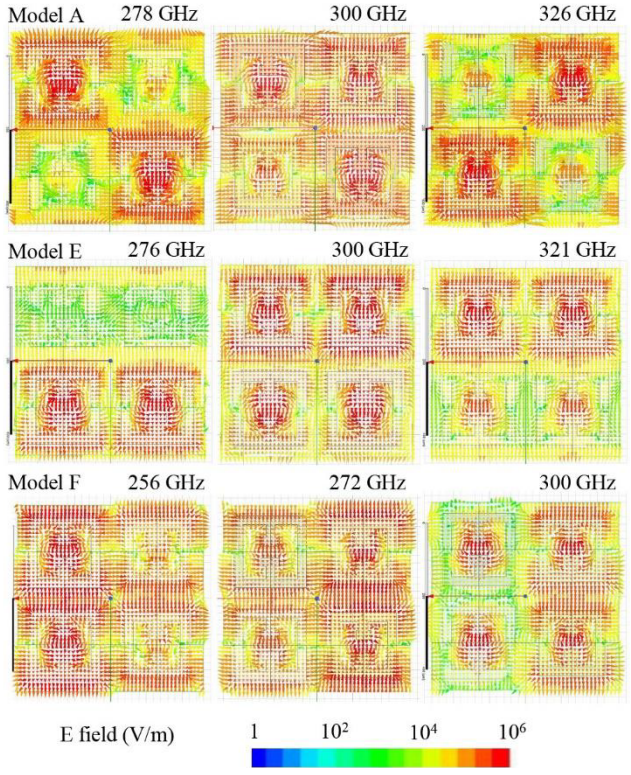

Fig. 13 Simulation results of E-field of Models A, E, and F along the line C-F shown in Fig. 6.

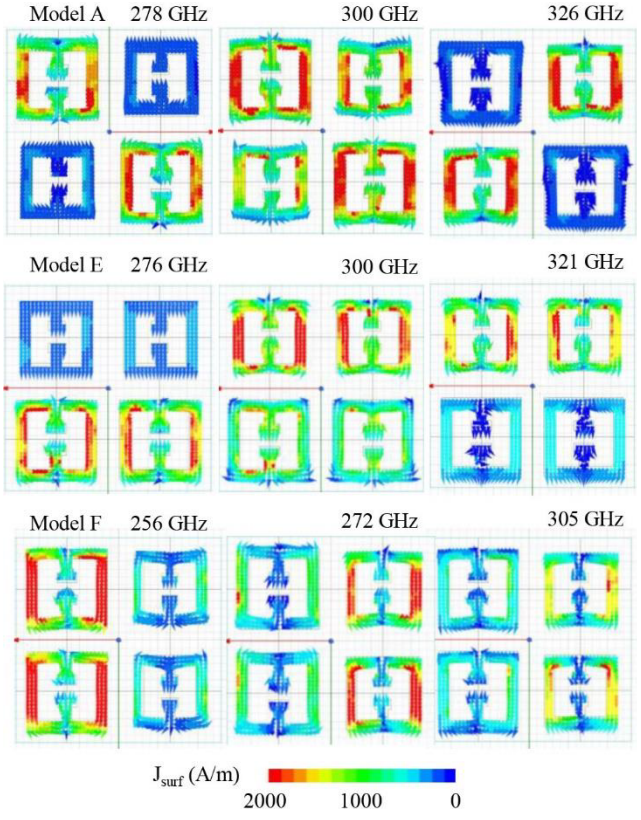

Fig. 14 Simulation results of the surface current flows of dual-band SRR bandstop filters (Models A, E, and F).

model F differ significantly from those of models A and D because of the difference in the resonance mode.

4. Conclusion

This paper presents a 300-GHz-band dual-band bandstop filter composed of SRR unit cells of two different sizes. The transmission characteristics of the dual-band bandstop filter depend on the distance between the two different sized unit cells and the arrangement of the two different sized SRR unit cells. When the unit cell size of the SRR is 220 μm, strong electric coupling between adjacent SRRs occurs, and the stopbands of the dual-band SRR bandstop filter are different from those of the single SRR unit cells that configure the dual-band bandstop filter. When the unit cell size of the SRRs exceeds 260 μm, the electric and magnetic coupling between the SRRs is weak, and the stopbands of the dual-band bandstop filter are almost the same as those of the single SRR unit cells that configure the dual-band bandstop filter. We designed a 300-GHz-band bandpass filter composed of two different sized SRR unit cells, and demonstrated that the insertion loss at 297 GHz was 1.8 dB, and the 3-dB passband became 16 GHz (290-306 GHz). In a dual-band bandstop filter with same sized SRRs aligned parallel to the field direction, strong electric coupling between SRRs of the same size results in magnetic coupling between the SRRs of different sizes. Consequently, the stopbands of the proposed dual-band bandstop filter are shifted significantly to the low-frequency side.

Acknowledgments

Part of this work was supported by MEXT KAKENHI (Grant number JP 21H01328).

References

[1] T. Schneider, A. Wiatrek, S. Preussler, M. Grigat, and R.-P. Braun, "Link Budget Analysis for Terahertz Fixed Wireless Links," IEEE Trans. THz Sci. Technol., vol.2, no.2, pp.250–256, 2012.
[2] S. Lee, S. Hara, T. Yoshida, S. Amakawa, R. Dong, A. Kasamatsu, J. Sato, and M. Fujishima, "An 80-Gb/s 300-GHz-Band Single-Chip CMOS Transceiver," IEEE J. Solid-State Circuits, vol.54, no.12, pp.3577–3588, 2019.
[3] M. Fujishima, "Coverage of Sub-Terahertz Communications and A 300-GHz-Band CMOS Transceiver," 2021 13th Global Symposium on Millimeter-Waves & Terahertz (GSMM), pp.1–3, 2021.
[4] S. Hara, K. Takano, K. Katayama, R. Dong, S. Lee, I. Watanabe, N. Sekine, A. Kasamatsu, T. Yoshida, S. Amakawa, and M. Fujishima, "300-GHz CMOS Transceiver for Terahertz Wireless Communication," 2018 Asia-Pacific Microwave Conference (APMC), Kyoto, Japan, pp.429–431, 2018.
[5] K. Takano, S. Amakawa, K. Katayama, S. Hara, R. Dong, A. Kasamatsu, I. Hosako, K. Mizuno, K. Takahashi, T. Yoshida, and M. Fujishima, "17.9 A 105Gb/s 300GHz CMOS transmitter," IEEE International Solid-State Circuits Conference (ISSCC), pp.308–309, Feb. 2017.
[6] A. Kasamatsu, "An Introduction to Japanese R&D projects on 300-GHz band Wireless Communications," 2020 45th International Conference on Infrared, Millimeter, and Terahertz Waves (IRMMW-THz), pp.1–2, 2020.

[7] A. Kamma, R. Das, and J. Mukherjee, "Multiple Band Notch Filter Using Contiguous Split Ring Resonators (SRR)," Asia-Pacific Microwave Conference (APMC), New Delhi, India, pp.1–4, 2016.
[8] H. Wang, W.-D. Hu, R.-T. Liu, L.-M. Si, J.-Y. Yin, and T. Dong, "A Design of 300 GHz Waveguide Bandpass Filter with H-plane Offset Inductive Window," 2016 IEEE 9th UK-Europe-China Workshop on Millimetre Waves and Terahertz Technol. (UCMMT), pp.189–191, 2016.
[9] N. Zhang, R. Song, M. Hu, G. Shan, C. Wang, and J. Yang, "A Low-Loss Design of Bandpass Filter at the Terahertz Band," IEEE Microwave and Wireless Components Lett., vol.28, no.7, pp.573–575, 2018.
[10] F. Wang, V.F. Pavlidis, and N. Yu, "Miniaturized SIW Bandpass Filter Based on TSV Technology for THz Applications," IEEE Trans. THz Sci. Technol., vol.10, no.4, pp.423–426, 2020.
[11] C.-P. Chen, T. Anada, S. Takeda, and Z. Ma, "Proposal and Theoretical Design of THz Bandpass Filters using Metallic Photonic Crystal Resonators," Proc. 46th European Microwave Conf., pp.116–119, 2016.
[12] F. Lan, Z. Yang, Z. Shi, and X. Tang, "Enhanced performance of THz bandpass filter based on bilayer reformative complementary structures," 2015 40th Int. Conf. on Infrared, Millimeter, and Terahertz waves (IRMMW-THz), pp.1–2, 2015.
[13] T.-T. Yeh, S. Genovesi, A. Monorchio, E. Prati, F. Costa, T.-Y. Huang, and T.-J. Yen, "Ultra-broad and sharp-transition bandpass terahertz filters by hybridizing multiple resonances mode in monolithic metamaterials," Optics Express, vol.20, no.7, pp.7580–7589, 2012.
[14] K. Lee, J. Son, J. Park, B. Kang, W. Jeon, F. Rotermund, and B. Min, "Linear frequency conversion via sudden merging of meta-atoms in time-variant metasurfaces," Nature Photonics, vol.12, no.12, pp.765–773, 2018.
[15] D. Schurig, J.J. Mock, and D.R. Smith, "Electric-field-coupled resonators for negative permittivity metamaterials," Appl. Phys. Lett. vol.88, no.4, 2006.
[16] W.J. Padilla, M.T. Aronsson, C. Highstrete, M. Lee, A.J. Taylor, and R.D. Averitt, "Electrically resonant terahertz metamaterials: Theoretical and experimental investigations," Phys. Rev. B, vol.75, no.4, 2007.
[17] J.D. Baena, J. Bonache, F. Martin, R.M. Sillero, F. Falcone, T. Lopetegi, M.A.G. Laso, J. Garcia-Garcia, I. Gil, M.F. Portillo, and M. Sorolla, "Equivalent-circuit models for split-ring resonators and complementary split-ring resonators coupled to planar transmission lines," IEEE Trans. Microw. Theory. Tec., vol.53, no.4, pp.1451–1461, April 2005.
[18] E.R. Afthar, M.R. Hidayat, and A. Munir, "Analysis of Equivalent Circuit for Bandpass Filter Based on SRR with Groundplane Windowing," Asia-Pacific Conf. on Communications, pp.361–364, 2016.
[19] M.K.T. Al-Nuaimi, and W. Whittow, "Compact Microstrip Band Stop Filter Using SRR and CSSR: Design, Simulation and Results," European Conf. on Antennas and Propag., pp.2–6, 2010.
[20] J. Bonache, I. Gil, J. Garcia-Garcia, and F. Martin, "Novel microstrip bandpass filters based on complementary split-ring resonators," IEEE Trans. Microwave Theory and Techniq., vol.54, no.1, pp.265–271, 2006.
[21] Y.D. Dong, T. Yang, and T. Itoh, "Substrate Integrated Waveguide Loaded by Complementary Split-Ring Resonators and Its Applications to Miniaturized Waveguide Filters," IEEE Trans. Microwave Theory and Techniq., vol.57, no.9, pp.2211–2223, 2009.
[22] C. Yiran, J. Long, Z. Zhengheng, and L. Lei, "Novel design of substrate integrated waveguide filter employing broadside-coupled complementary split ring resonators," IEICE Electron. Express, Vol.12, no.6, 2015.
[23] S.S. Karthikeyan, and R.S. Kshetrimayum, "Notched UWB bandpass filter using complementary single split ring resonator," IEICE Electron. Express, vol.7, no.17, pp.1290–1295, 2010.
[24] H. Tao, C.M. Bingham, A.C. Strikwerda, D. Pilon, D. Shrekenhamer, N.I. Landy, K. Fan, X. Zhang, W.J. Padilla, and R.D. Averitt, "Highly flexible wide angle of incidence terahertz metamaterial absorber: Design, fabrication, and characterization," Physical Review B, vol.78, no.24, 2008.
[25] Y. Kuo, W.Y. Yu, H. Ao, and Z. Xiao Qin, "Dual-band terahertz metamaterial absorber based on H-shape and double-SRR structure," 2015 IEEE International Conference on Communication Problem-Solving (ICCP), pp.200–203, 2015.
[26] W. Junlin, Z. Binzhen, W. XIN, and D. Junpin, "Flexible dual-band band-stop metamaterials filter for the terahertz region," Optical Material Express, vol.7, no.5, pp.1656–1665, 2017.
[27] K. Lee, J. Son, J. Park, B. Kang, W. Jeon, F. Rotermund, and B. Min, "Linear frequency conversion via sudden merging of resonances in time-variant metasurfaces," Nature Photonics, vol.12, pp.765–773, 2018.
[28] K. Itakura, A. Hirata, M. Sonoda, T. Higashimoto, T. Nagatsuma, T. Tomura, J. Hirokawa, N. Sekine, I. Watanabe, and A. Kasamatsu, "Control of 120-GHz-band split ring resonator filter by coupling lattice pattern substrate," IEICE Trans. Electron., vol.E104-C, no.3, pp.102–111, March 2020.
[29] A. Hirata, K. Itakura, T. Higashimoto, Y. Uemura, T. Nagatsuma, T. Tomura, J. Hirokawa, N. Sekine, I. Watanabe, and A. Kasamatsu, "Transmission characteristics control of 120 GHz-band bandstop filter by coupling alignment-free lattice pattern," IEICE Trans. Electron., vol.E104-C, no.10, pp.587–595, Oct. 2021.
[30] K. Luo, S.-H. Ge, L. Zhang, H.-B. Liu, and J.-L. Xing, "Simulation Analysis of Ansys HFSS and CST Microwave Studio for Frequency Selective Surface," 2019 International Conference on Microwave and Millimeter Wave Technology (ICMMT), pp.1–3, 2019.

Akihiko Hirata received his B.S. and M.S. degrees in chemistry and his Dr. Eng. degree in electrical and electronics engineering from Tokyo University, Tokyo, Japan, in 1992, 1994, and 2007, respectively. He joined the Atsugi Electrical Communications Laboratories of Nippon Telegraph and Telephone Corporation (presently NTT Device Technology Laboratories) in Kanagawa, Japan, in 1994. He was a senior research engineer and supervisor at NTT Device Technology Laboratories. He has been a professor at the Chiba Institute of Technology since 2016. His current research involves millimeter-wave antennas and ultra-broadband millimeter-wave wireless systems. Prof. Hirata is a senior member of IEEE and a senior member of IEICE.